Scientific Research Publishing

Atmospheric and Climate Sciences, 2025, 15(4), 890-907
https://www.scirp.org/journal/acs
ISSN Online: 2160-0422
ISSN Print: 2160-0414

Modeling of Ionospheric Response to Geomagnetic Storms over the East African Low Latitude Region Using Artificial Neural Networks

Vaola Agaba[1*], Valence Habyarimana[1], Sharon Aol[1], Tom Mutabazi[1], Vallence Niyonzima[2], Eugene Bizimana[3]

[1]Department of Physics, Mbarara University of Science and Technology, Mbarara, Uganda
[2]Department of Nursing, Mbarara University of Science and Technology, Mbarara, Uganda
[3]Department of Biomedical Engineering, Mbarara University of Science and Technology, Mbarara, Uganda
Email: *vaola3164@gmail.com

How to cite this paper: Agaba, V., Habyarimana, V., Aol, S., Mutabazi, T., Niyonzima, V. and Bizimana, E. (2025) Modeling of Ionospheric Response to Geomagnetic Storms over the East African Low Latitude Region Using Artificial Neural Networks. *Atmospheric and Climate Sciences*, **15**, 890-907.
https://doi.org/10.4236/acs.2025.154045

Received: September 1, 2025
Accepted: October 11, 2025
Published: October 14, 2025

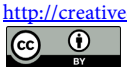

Abstract

Geomagnetic storms significantly disturb the ionosphere, impacting satellite-based systems such as the Global Navigation Satellite System (GNSS), communication links, and power infrastructure. This study models the ionospheric response to geomagnetic storms over East Africa using GNSS-derived Total Electron Content (TEC) data from five International GNSS Service (IGS) stations during solar cycle 24 (2008-2019). We identified geomagnetic storms using the criteria of Disturbance storm time $(\mathrm{Dst}) \leq -30\mathrm{nT}$ and $\mathrm{kp} \geq 3$, yielding 802 events, of which 787 were CIR-driven and 15 CME-driven. To determine the optimal background method for ionospheric storm extraction, five approaches were tested. The monthly median vertical TEC (VTEC) method provided the best performance (Root mean square error, RMSE = 26.42 TECU; Mean absolute error, MAE = 17.10 TECU), while the five internationally quietest days gave the least performance (RMSE = 50.82 TECU; MAE = 30.96 TECU). We then developed a storm-time Artificial Neural Network (ANN) model for ionospheric storms. The inputs include solar activity factor ($F_{10.7P}$), hour of day (HR), day of year (DOY), latitude, longitude, z-component of the interplanetary magnetic field (IMF Bz), and Dst index, representing solar, diurnal, seasonal, spatial, and geomagnetic dependencies. The output was ΔVTEC, with storm conditions defined as deviations with a magnitude greater than 45%. The optimum ANN model had a configuration of 9 inputs, 16 hidden neurons, 1 output, with an RMSE of 23.49%. The ANN model performance was robust under high solar activity and quiet to moderate

geomagnetic conditions with an average RMSE of 23% and MAE of 16.5%, though errors increased during intense geomagnetic storm periods. These results demonstrate that ANN models can reliably capture diurnal and seasonal ionospheric variability in East Africa and provide a foundation for regional space weather forecasting and mitigation strategies.

Keywords

Geomagnetic Storms, Ionospheric Response, Total Electron Content (TEC), Space Weather, Ionospheric Modeling, Artificial Neural Networks (ANNs)

1. Introduction

The Sun, the dominant driver of space weather, continuously emits a stream of charged particles known as solar wind [1]-[3]. The solar wind is composed mainly of electrons and protons, flowing outward from the solar corona with typical velocities of about 400 km/s and densities near 5 particles/cm^3 [1] [4]. Embedded within this plasma flow is the interplanetary magnetic field (IMF), an extension of the solar magnetic field carried into space [1] [3]. Variations in solar wind properties, particularly during active solar periods, strongly influence the Earth's magnetosphere leading to geomagnetic storms [5]. The average IMF magnitude near the Earth is about 5 nT, though it can increase significantly during eruptive solar events [3]. The two main solar drivers of geomagnetic storms are Coronal Mass Ejections (CMEs) and Corotating Interaction Regions (CIRs) [6]-[8]. The CMEs are large-scale expulsions of magnetized plasma from the solar corona, frequently associated with solar flares, and are primary drivers of severe geomagnetic storms. Their propagation speeds range from 100 to over 2000 km/s [9] [10]. When the southward IMF component reaches the Earth, strong magnetospheric coupling can trigger intense geomagnetic activity [3] [11]. The CIRs, on the other hand, arise at the boundary between fast and slow solar wind streams, usually during the declining and minimum phases of the solar cycle. They recur with solar rotation and can persist for several days. Although generally less intense than CME-driven storms, CIRs are capable of generating moderate but long-lasting geomagnetic activity [10] [12] [13].

Geomagnetic storms are temporary disturbances in the Earth's magnetosphere, caused by enhanced energy transfer from the solar wind into the magnetosphere, primarily when southward IMF Bz interacts with the Earth's magnetic field via magnetic reconnection [14] [15]. The concept of geomagnetic storms was first introduced by Humboldt [16], who linked geomagnetic disturbances to auroral activity. During geomagnetic storms, oppositely drifting protons and electrons form the ring current, weakening the geomagnetic field as observed at the surface [17] [18]. Geomagnetic activity is quantified using indices such as Disturbance storm time (Dst), Symmetric Horizontal component of the Earth's magnetic field (Sym-H), planetary k index (kp), Auroral electrojet (AE), and planetary A

(Ap) index, which track various aspects of magnetospheric and ionospheric variability [15] [19]. Based on Dst, storms are categorized as weak ($-30 \geq \text{Dst} > -50$ nT), moderate ($-50 \geq \text{Dst} > -100$ nT), strong ($-100 \geq \text{Dst} > -200$ nT), intense ($-200 \geq \text{Dst} > -300$ nT), and severe ($\text{Dst} \leq -300$ nT) [15] [18]. Geomagnetic storms can cause significant disturbances in the ionosphere (ionospheric perturbations), adversely affecting satellite communications, GNSS navigation, and other space-based technologies [20]. The intensity and temporal evolution of these ionospheric perturbations exhibit substantial regional variability. While numerous studies have investigated storm-time ionospheric responses at mid- and high-latitudes (e.g., [6] [10] [21]-[23]), the low-latitude ionosphere over East Africa remains poorly characterized. This region is particularly complex due to its unique electrodynamic environment, making it especially susceptible to space weather effects. The scarcity of regional studies limits the ability to accurately forecast ionospheric conditions and implement effective mitigation strategies for space-based systems in this part of the world.

Storm-time energy deposition produces profound effects on the ionosphere, particularly at low and mid-latitudes. These include Prompt Penetration Electric Fields (PPEFs), equatorward neutral winds, and thermospheric composition changes [24]-[27]. The primary observable parameter affected is the Total Electron Content (TEC), defined as the total number of electrons in a 1 m^2 column along a GNSS signal path [28] [29], with 1 TEC unit (TECU) equivalent to 10^{16} electrons/m^2 [30]. Positive storm effects, expressed as TEC enhancements, are associated with penetration electric fields and equatorial anomaly intensification [31], while negative effects, marked by TEC depletion, result from changes in thermospheric composition, equatorward winds, and inhibited plasma uplift [32]-[35]. These ionospheric disturbances degrade GNSS accuracy, cause navigation errors, and may even contribute to power grid failures [36]-[39].

Numerous studies have examined ionospheric storm responses globally and regionally. For example, Habarulema *et al.* [40] carried out a comparative study of TEC response for the African equatorial and mid-latitudes during two successive ionospheric storms of 7-12 November 2004. They observed negative storm effects over both mid and equatorial latitudes during the recovery phase and a shift in equatorial TEC enhancement that was partially attributed to passage of Travelling Ionospheric Disturbances (TIDs). Matamba *et al.* [6] carried out a statistical analysis of ionospheric response over two ionosonde stations in South Africa during geomagnetic storm conditions which occurred between 1996-2011. Their results showed a strong solar cycle dependence with negative ionospheric storm effects following the solar cycle and positive ionospheric storm effects occurring most frequently during solar minimum. In addition, negative and positive ionospheric storm effects occurred most in summer. Only negative ionospheric storms were observed during great geomagnetic storm activity ($\text{Dst} \leq -350$ nT). Tshisaphungo *et al.* [41] modeled ionospheric response during geomagnetic storms using Artificial Neural Networks (ANNs) and linear regression techniques. They found out

that both ANNs and linear regression models were capable of capturing the ionospheric critical frequency of the F2 layer (foF2) responses during two great geomagnetic storms of 28 October-1 November 2003 and 6-12 November 2004. Despite these advances, the East African low-latitude region remains understudied, although it is characterized by unique electrodynamics, including strong equatorial anomaly development and complex geomagnetic conditions. Besides, regional ionospheric models that incorporate local drivers are generally more accurate than global models for predicting storm-time behavior [42]. This study aims to model the ionospheric response to geomagnetic storms over East Africa using GNSS-derived TEC data and ANNs for the years from 2008 to 2019.

2. Data and Methods

2.1. Data

The GNSS-derived TEC data were obtained from Receiver INdependent EXchange (RINEX) observation files archived at https://data.unavco.org/archive/gnss/rinex/obs/ for solar cycle 24. Data were downloaded for the five IGS stations along the East African sector. The stations used in this study and their coordinates are given in Table 1.

Table 1. Geographic and geomagnetic coordinates of selected IGS stations in East Africa.

Station Name	Station code	Geographic coordinates		Geomagnetic coordinates	
		Longitude (˚)	Latitude (˚)	Longitude (˚)	Latitude (˚)
Mbarara	MBAR	30.70	−0.61	101.27	10.23
Malindi	MAL2	40.19	−3.22	111.35	6.92
Addis Ababa	ADIS	38.80	9.03	109.87	0.72
Dodoma	DODM	35.75	−6.17	106.47	8.44
Kigali	NURK	30.09	−1.95	101.09	9.83

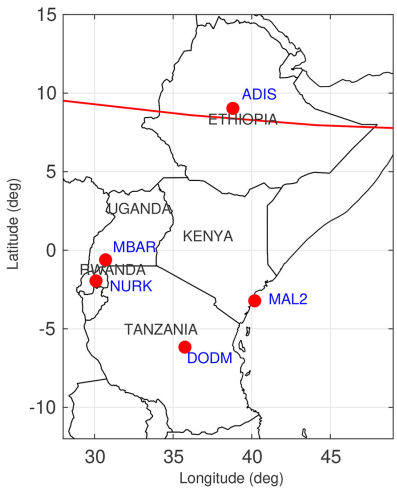

Figure 1. Geographical distribution of the IGS stations used in this study. The red solid curve is the geomagnetic equator. The red circle indicates the location of the IGS station.

Figure 1 shows the geographical locations of the stations used in this study. The TEC values were extracted from the RINEX files using the GPS-TEC algorithm developed at Boston College [43]. To reduce multipath effects while retaining high quality data, only observations from satellites with elevation angles above 30˚ were considered [25] [44]-[46]. Data for the geomagnetic activity indices were downloaded from the World Data Center for Geomagnetism, Kyoto in Japan (http://wdc.kugi.kyoto-u.ac.jp/dstae/index.html). Solar activity ($F_{10.7}$), IMF Bz, and kp index data were downloaded from https://omniweb.gsfc.nasa.gov/form/dx1.html. The adjusted solar flux (solar activity factor), $F_{10.7P}$ was used since it better represents solar activity for ionospheric modeling [47] and was computed using Equation (1):

$$F_{10.7P} = \frac{F_{10.7} + F_{10.7_{81}}}{2}, \tag{1}$$

where $F_{10.7_{81}}$ is the 81-day running mean of F10.7.

2.2. Methods

2.2.1. Identification of Geomagnetic Storms and the Best Background Method

Geomagnetic storm periods were identified using the $\mathrm{Dst} \le -30$ nT and $\mathrm{kp} \ge 3$ [10]. These were then classified as either CME- or CIR-driven according to their Dst profiles [12] [48] [49]. The CME-driven storms were defined by Dst minima below −100 nT, while CIR-driven storms typically exhibited moderate Dst depressions (−25 to −100 nT). Sustained storm-time conditions were confirmed using the six-hour consecutive pattern, reducing false detection from transient variations [50] [51]. To ensure sustained storm conditions, six consecutive hourly Dst values (five 1-hour differences) were used. The percentage deviation of TEC (ΔVTEC) from a selected background was computed using Equation (2) [8] [52]:

$$\Delta\mathrm{VTEC} = \frac{\mathrm{VTEC} - \mathrm{VTEC}_k}{\mathrm{VTEC}_k} \times 100\%, \tag{2}$$

where VTEC_k represents the background VTEC obtained using different methods. The background VTEC used in this study included the monthly median (MM), seven-day median before storm (M7), quiet day before and after storm (QBA), quiet day before sudden storm commencement (QSSC), and five internationally quietest days (FIQD) (e.g., [6] [25] [30] [31] [35] [46] [53] [54]). A threshold of ±45% was used to define ionospheric storm conditions, reflecting greater variability in low-latitude regions compared to mid-latitudes [6] [52]. The suitability of background methods was assessed based on root mean square error (RMSE) and mean absolute error (MAE) using Equation (3) and Equation (4), respectively [8] [55]:

$$\mathrm{RMSE} = \sqrt{\frac{1}{N}\sum_{i=1}^{N}\left(\mathrm{VTEC}_{\mathrm{actual}} - \mathrm{VTEC}_{\mathrm{background}}\right)^2}, \tag{3}$$

$$\mathrm{MAE} = \frac{1}{N}\sum_{i=1}^{N}\left|\mathrm{VTEC}_{\mathrm{actual}} - \mathrm{VTEC}_{\mathrm{background}}\right|. \quad (4)$$

The background method that yielded the lowest RMSE and MAE was taken as the best and used to compute ΔVTEC during ANN model development.

2.2.2. Modeling Ionospheric Response Using ANNs

The percentage TEC deviations (ΔVTEC) were used as a proxy of ionospheric response and modeled using ANNs. ANNs are capable of learning complex input-output relationships from data [41] [46] [56]. The model inputs included $F_{10.7P}$, hour of day (HR), day of year (DOY), LON, LAT, $F_{10.7P}$, IMF-Bz and Dst index. The output was ΔVTEC. Equation (5) shows the overall model.

$$\Delta\mathrm{VTEC} = \Delta\mathrm{VTEC}\left(\mathrm{HR}, \mathrm{DOY}, \mathrm{LON}, \mathrm{LAT}, \mathrm{F}_{10.7\mathrm{P}}, \mathrm{Bz}, \mathrm{Dst}\right). \quad (5)$$

Temporal parameters (HR and DOY) were transformed into Fourier components to account for diurnal and annual periodicities, using Equation (6):

$$\begin{aligned} \mathrm{doyc} &= \cos\left(\frac{2\pi\times\mathrm{DOY}}{365.25}\right), \quad \mathrm{Hrc} = \cos\left(\frac{2\pi\times\mathrm{HR}}{24}\right), \\ \mathrm{doys} &= \sin\left(\frac{2\pi\times\mathrm{DOY}}{365.25}\right), \quad \mathrm{Hrs} = \sin\left(\frac{2\pi\times\mathrm{HR}}{24}\right). \end{aligned} \quad (6)$$

LAT and LON in Equation (5) represent the latitude and longitude of the Ionospheric Pierce Point (IPP), where the satellite-receiver line-of-sight intersects the ionospheric shell. To evaluate the model performance, we used RMSE in Equation (3) and normalized RMSE (NRMSE) computed using Equation (7):

$$\mathrm{NRMSE} = \frac{\mathrm{RMSE}}{\Delta\mathrm{VTEC}_{\mathrm{max}} - \Delta\mathrm{VTEC}_{\mathrm{min}}}, \quad (7)$$

where $\Delta\mathrm{VTEC}_{\mathrm{max}}$ and $\Delta\mathrm{VTEC}_{\mathrm{min}}$ are the extreme values of percentage deviation.

2.2.3. Model Training and Validation

We trained the ANN model on data from 2008-2009, 2011-2013, and 2015-2019, with hidden neurons varying from 1 to 40. The ANN model was then validated using independent dataset for the years 2010 (solar minimum) and 2014 (solar maximum) that were excluded from the training dataset to assess the model's ability to generalize under different solar activity conditions. The model configuration with the lowest RMSE was selected as the optimum model. The selected ANN model was then used to evaluate ΔVTEC under various geophysical and geomagnetic conditions such as solar activity, geomagnetic storm intensity, IMF polarity, diurnal variation, and seasonal dependence. The RMSE and MAE values were computed across these conditions to provide a comprehensive evaluation of the model performance.

3. Results and Discussion

3.1. Characterization of Geomagnetic Storms

Geomagnetic storms were classified based on their solar wind drivers. The CME-

driven storms were associated with Dst minima below −100 nT, while CIR-driven storms had Dst depressions between −25 and −100 nT sustained for at least six consecutive hours. Figure 2 shows the annual distribution of CIR- and CME-driven storms during solar cycle 24. A total of 802 storms were identified, of which 787 were CIR-driven and 15 were CME-driven.

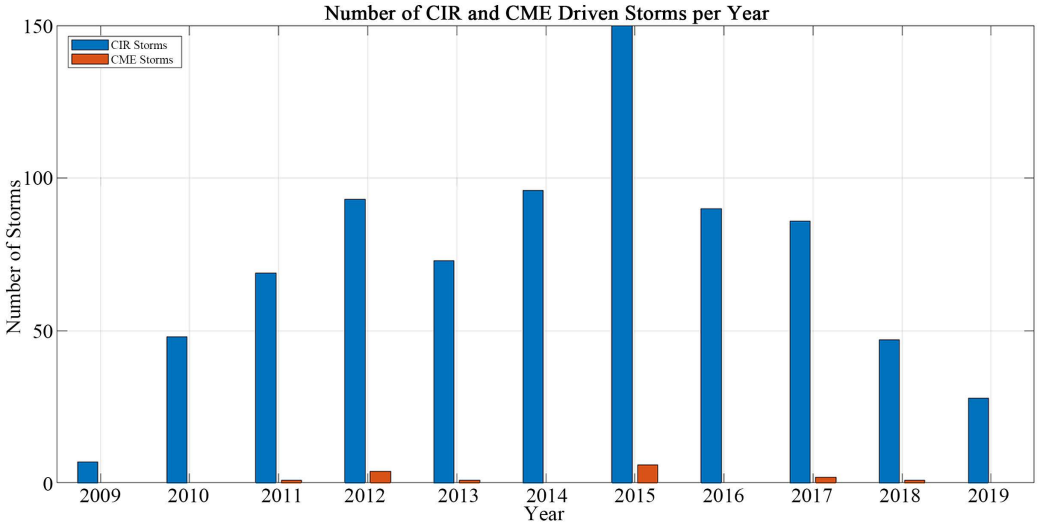

Figure 2. Number of CIR and CME driven storms per year between 2009-2019 a period of solar cycle 24.

Three representative geomagnetic storms were selected for detailed analysis; one strong CME-driven event (2015, DOY 77) and two CIR-driven storms (2018, DOY 238; 2010, DOY 46). Their key characteristics including Dst index, IMF Bz, solar wind speed, density, temperature, kp index, and dynamic pressure are summarized in Table 2. The CME-driven storms exhibited abrupt and intense geomagnetic responses, whereas CIR-driven storms were moderate, gradual, and influenced by high-speed streams and dynamic pressure, consistent with the findings by Borovsky and Denton [57].

Table 2. Characterization of the selected geomagnetic storms in 2010, 2015 and 2018.

Storm Type	Year	DOY	Hour	Dst min (nT)	Bz (nT)	Temp (K)	Density (cm^{-3})	Speed (km/s)	Kp	P
CME (Strong)	2015	77	0	−200.0	−5.7	137151	6.4	591	6	5.32
CIR (Moderate)	2018	238	13	−94.0	+0.9	196032	17.4	424	4.7	6.02
CIR (Weak)	2010	46	1	−28.0	−6.7	33071	7.8	313	3	1.62

3.2. Selection of the Best Background Estimation Method

To estimate the best ionospheric background technique during geomagnetic storm conditions, five methods were implemented. These included monthly median (MM), seven-day median before storm (M7), quiet day before and after storm (QBA), quiet day before sudden storm commencement (QSSC), and five internationally quietest days (FIQD). These methods were applied to hourly VTEC data to estimate the background VTEC values, which were compared to

storm-time observations to compute RMSE and MAE evaluation metrics. To conserve space and to cater for each storm category, eight geomagnetic storm periods were selected to represent a range of solar, seasonal, and diurnal conditions. The selected geomagnetic storms included 2010 (DOY 362-364), 2011 (DOY 152-154), 2012 (DOY 24-26), 2014 (DOY 232-234, 60-62), and 2015 (DOY 76-78, 287-289, 317-319). These events captured different seasons, including solstices and equinoxes, and varied solar cycle phases. Figure 3 illustrates the VTEC estimates from each method against observations, with percentage deviations.

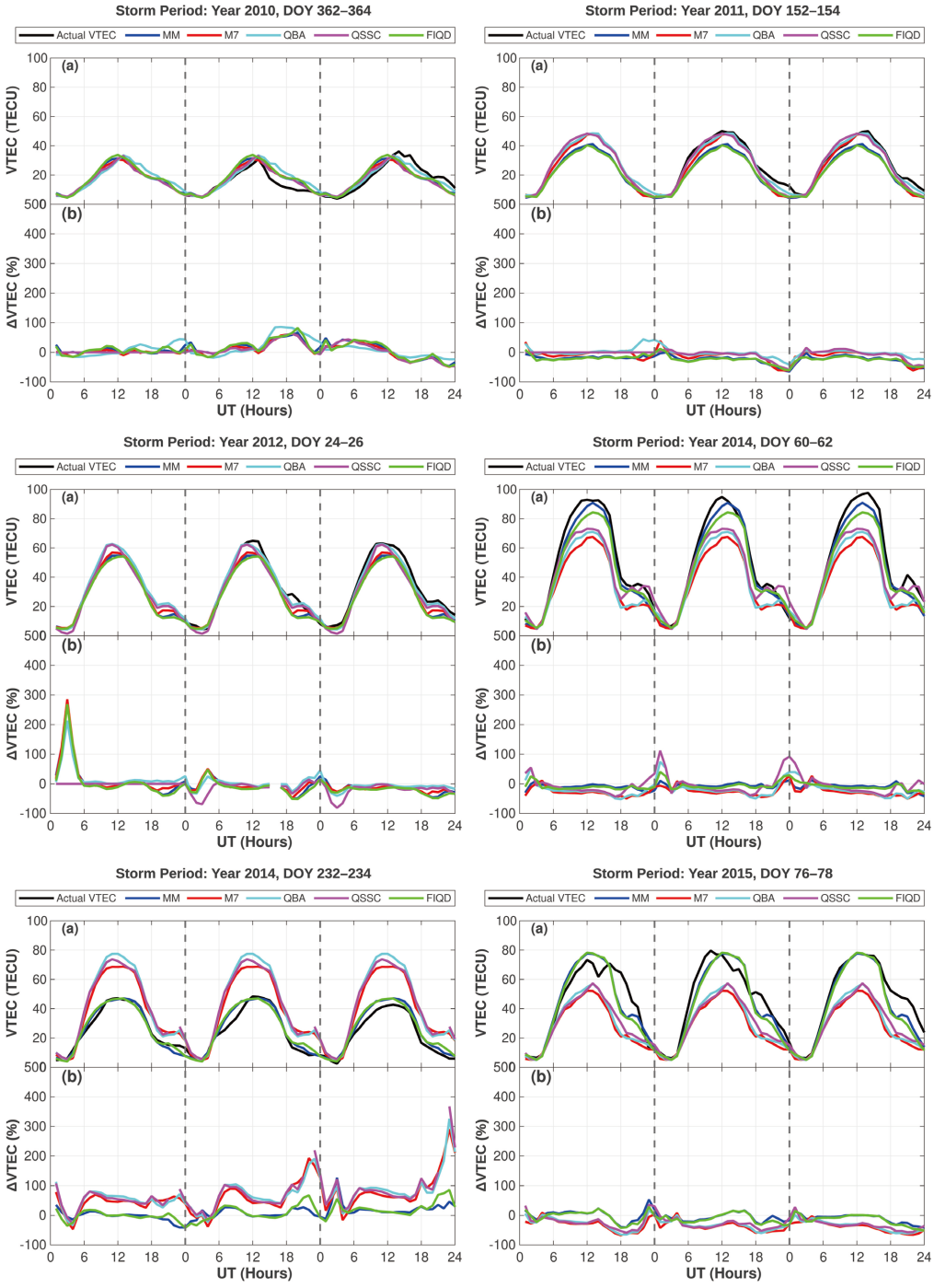

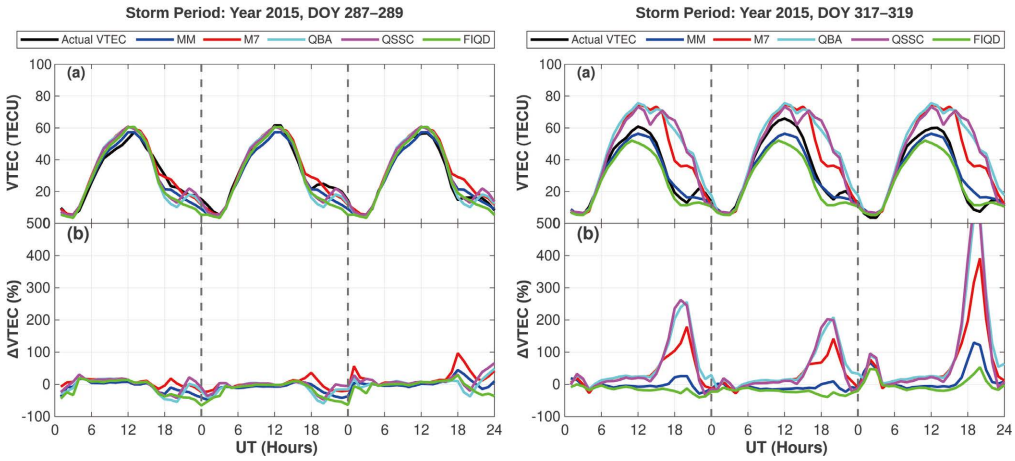

Figure 3. Selected geomagnetic storm periods among those used to evaluate the background estimation methods over the East African low-latitude region.

From **Figure 3**, it can be seen that the MM and QSSC background methods provide the most consistent estimates across all conditions. For instance, during the 2010 December solstice, all methods performed similarly, whereas in the 2014 September equinox, QBA overestimated peak VTEC values. Overall, MM recorded the lowest RMSE (26.42 TECU) and MAE (17.10 TECU), while FIQD had the highest errors, suggesting that globally geomagnetically quiet days may not necessarily represent optimal storm-time backgrounds in the East African equatorial region. **Table 3** shows the statistical comparison of the five background estimation methods. These findings corroborate earlier studies, such as Habarulema *et al.* [58], and highlight the need for adaptive or data-driven background models in future research, especially over the region of interest.

Table 3. Statistical comparison of background estimation methods using RMSE and MAE.

Method	RMSE (TECU)	MAE (TECU)
MM	**26.42**	**17.10**
M7	46.75	32.82
QBA	40.60	28.43
QSSC	42.06	27.41
FIQD	50.82	30.96

3.3. Modeling of the Ionospheric Response

We trained the ANNs model using data from 2008-2009, 2011-2013, and 2015-2019 with 2010 and 2014 reserved for validation. We then configured the model by varying the number of hidden neurons between 1 and 40 at an increment of one hidden neuron at a time, and calculated the RMSE for each model. The optimal performance (RMSE = 23.49%, MAE = 16.81%) was achieved with 9 inputs, 16 hidden neurons and 1 output. **Figure 4** presents the RMSE across neuron configurations for each model. To validate the performance of the model, we used selected events and compared the modeled and actual ΔVTEC values. **Figure 5**

displays modeled versus actual ΔVTEC for selected events. Model validation against observed ΔVTEC during representative storms showed reasonable agreement. The model captured general trends but underestimated rapid enhancements, particularly during intense daytime storms or PPEF events, reflecting limitations in simulating short-term electrodynamic processes.

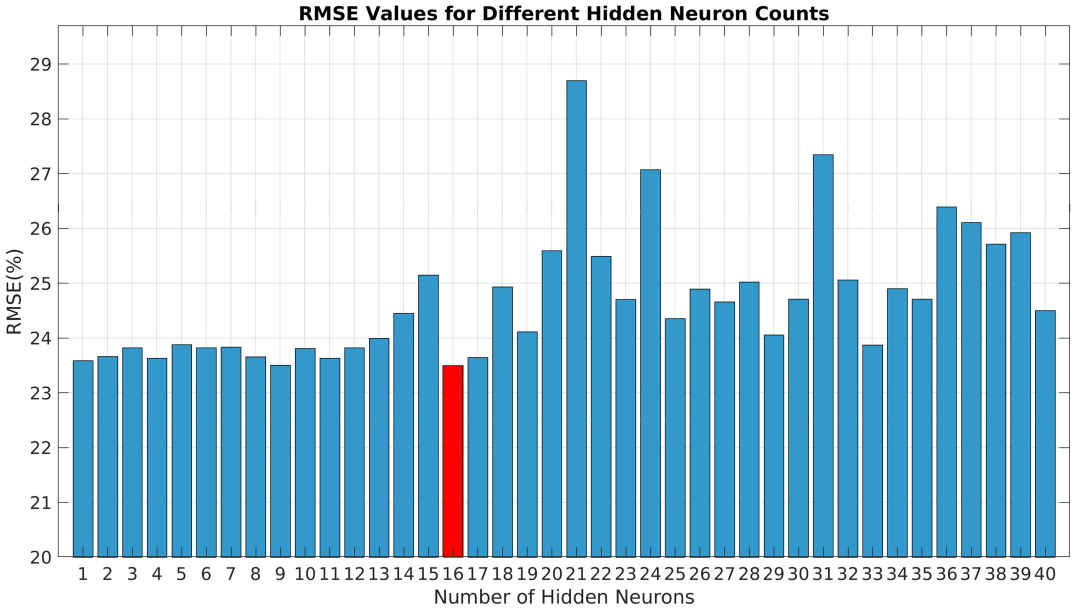

Figure 4. A bar graph showing the RMSE (%) for the different numbers of hidden neurons between 1 and 40.

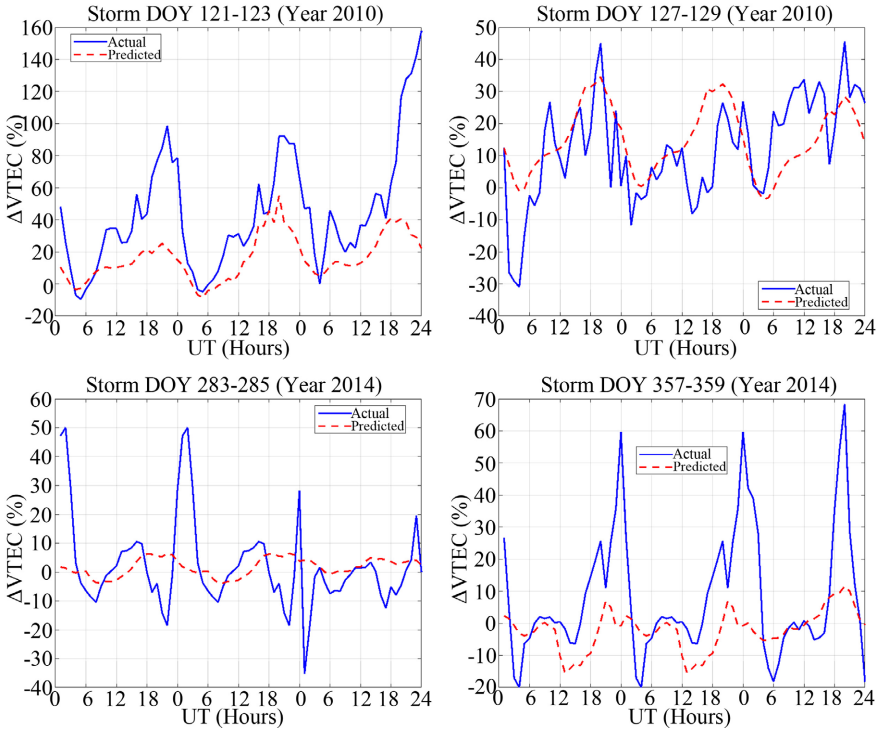

Figure 5. Actual and modeled ΔVTEC for representative geomagnetic storm periods used for model validation.

3.4. Model Performance under Various Physical and Geophysical Conditions

The model accuracy was evaluated across conditions of solar activity, geomagnetic intensity, IMF orientation, time of day, and seasonal variations. Figure 6 shows the seasonal dependence of daily mean ΔVTEC as a function of days of a year. The daily mean ΔVTEC revealed higher variability during 2010 (solar minimum) compared to 2014 (solar maximum), suggesting a solar cycle influence on the model performance. To reveal the diurnal dependence of ΔVTEC, mean hourly values of ΔVTEC were used for the validation dataset. Figure 7 shows the diurnal variation of ΔVTEC for different hours of the day. It can be seen from Figure 7 that modeled ΔVTEC exhibited underestimation between 03-18 UT, with best performance near midnight and late evening, consistent with reduced ionospheric variability during these hours. The model accuracy improved during solar maximum (2014), with lower RMSE (22.87%) and MAE (16.13%) compared to solar minimum (2010), where RMSE reached 23.77% as shown in Table 4. The ANN model benefits from the pronounced ionospheric variability during active solar periods, enhancing predictability.

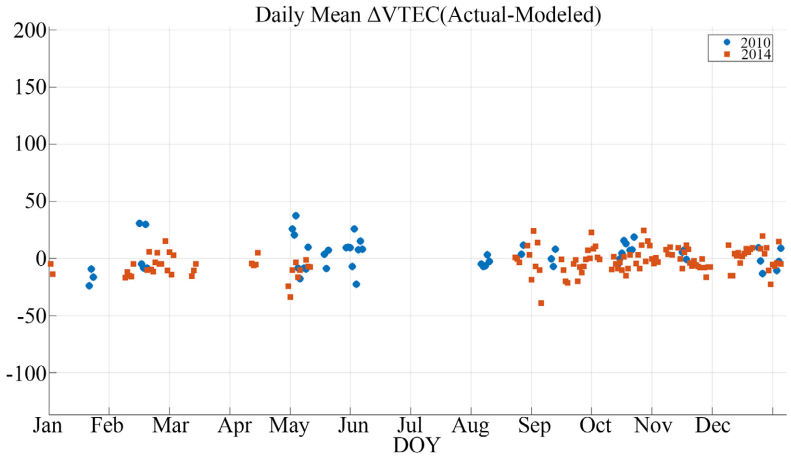

Figure 6. Seasonal dependence of the ionospheric response as a function of day of the year.

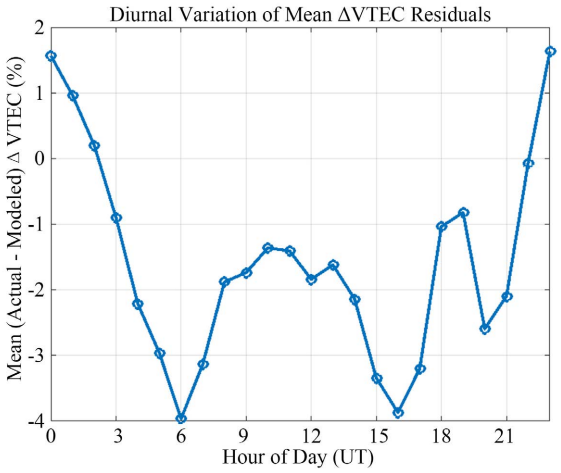

Figure 7. Diurnal variation of the ionospheric response as a function of hour of the day.

Table 4. Model performance under solar minimum (2010) and maximum (2014) conditions.

Year	RMSE (%)	MAE (%)
(Solar Minimum)	23.77	17.36
(Solar Maximum)	**22.87**	**16.13**
Combined (2010 and 2014)	23.49	16.81

The overall results for the model performance during different physical and geophysical conditions are presented in Figure 8 and summarized in Table 5 using RMSE and MAE as evaluation metrics. Performance was the highest during daytime and quiet geomagnetic periods, while nighttime and storm-time conditions posed deterioration in performance. Seasonal patterns indicated better performance during solstice periods than during equinoxes.

Table 5. Model validation across geophysical and geomagnetic conditions.

Condition	Samples	RMSE (%)	MAE (%)
Low Solar Activity	3056	23.77	17.36
High Solar Activity	14326	22.87	16.13
Quiet Geomagnetic	9542	22.65	16.26
Moderate Geomagnetic	18368	23.51	16.64
Storm-time	1997	27.08	20.93
Southward IMF	16926	23.62	16.95
Northward IMF	12614	23.37	16.63
Daytime	14986	16.21	12.20
Nighttime	14921	29.03	21.43
Equinox	5813	24.94	17.51
Solstice	256	22.72	16.94

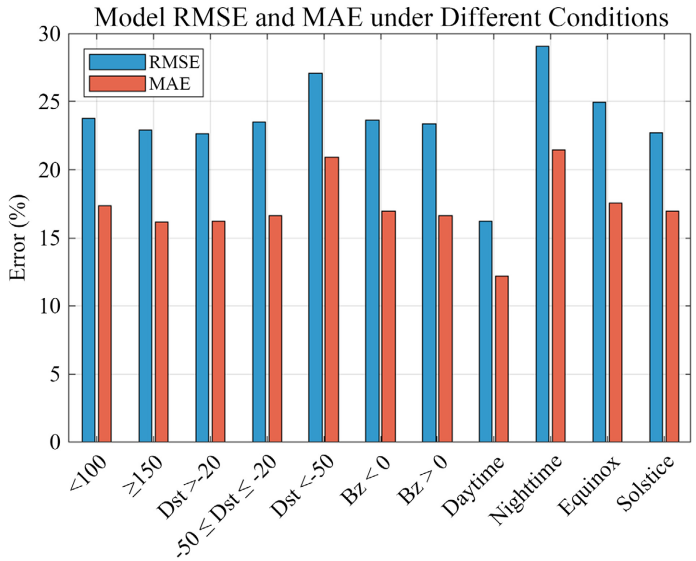

Figure 8. A bar graph of the model's RMSE and MAE under different geophysical and geomagnetic conditions.

4. Conclusion

In this study, ionospheric response to geomagnetic storms was modeled using GNSS-derived Total Electron Content (TEC) data from five International GNSS Service (IGS) stations over East Africa during solar cycle 24 (2008-2019). Geomagnetic storms were identified using the criteria of $\mathrm{Dst} \le -30$ nT and $\mathrm{kp} \ge 3$, yielding 802 events, of which 787 were CIR-driven and 15 were CME-driven. The optimal background method for ionospheric storm extraction was determined out of the five approaches which included the monthly median (MM), seven-day median before storm (M7), quiet day before and after storm (QBA), quiet day before sudden storm commencement (QSSC), and five internationally quietest days (FIQD). The MM provided the best performance with an RMSE of 26.42 TECU and MAE of 17.10 TECU. The best background estimate was then used to extract the ionospheric response representation (ΔVTEC) that was used as an output for the Artificial Neural Network (ANN) model. The model inputs included solar activity factor ($F_{10.7P}$), hour of day (HR), day of year (DOY), latitude, longitude, z-component of the interplanetary magnetic field (IMF Bz), and Disturbance storm time (Dst) index, representing solar, diurnal, seasonal, spatial, and geomagnetic dependencies. The optimum ANN model had a configuration of 9 inputs, 16 hidden neurons, and 1 output with a root mean square error (RMSE) of 23.49%. The ANN model performance was robust under high solar activity and quiet to moderate geomagnetic conditions with an average RMSE of 23% and mean absolute error (MAE) of 16.5%, though errors increased during intense geomagnetic storm periods. Model validation during representative storms showed reasonable agreement. The model captured general trends but underestimated rapid enhancements, particularly during intense daytime storms or PPEF events, reflecting limitations in simulating short-term electrodynamic processes. The modeled ΔVTEC exhibited underestimation between 03 - 18 UT, with the best performance near midnight and late evening, consistent with reduced ionospheric variability during these hours. The model accuracy improved during solar maximum (2014), with lower RMSE (22.87%) and MAE (16.13%) compared to solar minimum (2010), where RMSE reached 23.77%. Overall, the model performance was the highest during daytime and quiet geomagnetic periods, while nighttime and storm-time conditions posed deterioration in performance. Seasonal patterns indicated better performance during solstice periods than during equinoxes.

Author Contributions

VA and VH prepared the manuscript. VA, VH, SA, TM, VN, and EB designed and conducted the current research. VA and VH carried out the data analysis. VA interpreted the results and edited the draft manuscript together with VH, SA, TM, VN, and EB. All authors read and approved the final manuscript.

Availability of Data and Materials

All data is publicly available on their corresponding websites.

Acknowledgements

We acknowledge the government of Uganda through the Directorate of Research and Graduate Training (DRGT) of Mbarara University of Science and Technology for the funding. We thank the International GNSS Service (IGS) for providing the GNSS RINEX observation data used in this study (https://data.unavco.org/archive/gnss/rinex/obs/). We also thank the World Data Center for Geomagnetism, Kyoto, for providing the Dst index data (http://wdc.kugi.kyoto-u.ac.jp/dstae/index.html), and the NASA OMNIWeb team for access to solar and interplanetary parameters including $F_{10.7}$, IMF Bz, and Kp index (https://omniweb.gsfc.nasa.gov/form/dx1.html). We acknowledge the developers of the GPS-TEC algorithm at Boston College for enabling the extraction of Total Electron Content (TEC) from RINEX files. Finally, the authors appreciate the constructive feedback from the reviewers, which helped improve the quality of this manuscript.

Conflicts of Interest

The authors declare that they have no competing interests.

References

[1] Manoharan, P.K. (2003) The Solar Wind. In: *Lectures on Solar Physics*, Springer, 299-326.

[2] Schwenn, R. (2006) Space Weather: The Solar Perspective. *Living Reviews in Solar Physics*, **3**, 1-72. https://doi.org/10.12942/lrsp-2006-2

[3] Moldwin, M. (2008) An Introduction to Space Weather. Cambridge University Press. https://doi.org/10.1017/cbo9780511801365

[4] Russell, C.T. (2013) Solar Wind and Interplanetary Magnetic Field: A Tutorial. In: Song, P., Singer, H.J. and Siscoe, G.L., Eds., *Space Weather*, American Geophysical Union, 73-89. https://doi.org/10.1029/gm125p0073

[5] McPherron, R.L. (2005) Magnetic Pulsations: Their Sources and Relation to Solar Wind and Geomagnetic Activity. *Surveys in Geophysics*, **26**, 545-592. https://doi.org/10.1007/s10712-005-1758-7

[6] Matamba, T.M., Habarulema, J.B. and McKinnell, L. (2015) Statistical Analysis of the Ionospheric Response during Geomagnetic Storm Conditions over South Africa Using Ionosonde and GPS Data. *Space Weather*, **13**, 536-547. https://doi.org/10.1002/2015sw001218

[7] Dugassa, T. and Habyarimana, V. (2025) Ionospheric Disturbances in the African Low-Latitude Region during the Space Weather Event of September 2017. *Astrophysics and Space Science*, **370**, Article No. 18. https://doi.org/10.1007/s10509-025-04407-w

[8] Niwamanya, D., Habyarimana, V. and Jurua, E. (2025) Analysis of Geomagnetic Storm Effects on Ionospheric Vertical Drifts over the East African Low Latitude Region. *Atmospheric and Climate Sciences*, **15**, 373-390. https://doi.org/10.4236/acs.2025.152019

[9] Hundhausen, A.J. (1997) Coronal Mass Ejections. Geophysical Monograph Series, 99. https://doi.org/10.1029/gm099p0001

[10] Matamba, T.M. and Habarulema, J.B. (2018) Ionospheric Responses to CME- and CIR-Driven Geomagnetic Storms along 30°E-40°E over the African Sector from 2001 to 2015. *Space Weather*, **16**, 538-556. https://doi.org/10.1029/2017sw001754

[11] Webb, D.F. and Howard, T.A. (2012) Coronal Mass Ejections: Observations. *Living Reviews in Solar Physics*, **9**, 1-83. https://doi.org/10.12942/lrsp-2012-3

[12] Tsurutani, B.T. and Gonzalez, W.D. (1997) The Interplanetary Causes of Magnetic Storms: A Review. In: Tsurutani, B.T., Gonzalez, W.D., Kamide, Y. and Arballo, J.K., Eds., *Magnetic Storms*, American Geophysical Union, 77-89. https://doi.org/10.1029/gm098p0077

[13] Heber, B., Sanderson, T.R. and Zhang, M. (1999) Corotating Interaction Regions. *Advances in Space Research*, **23**, 567-579. https://doi.org/10.1016/s0273-1177(99)80013-1

[14] Dungey, J.W. (1961) Interplanetary Magnetic Field and the Auroral Zones. *Physical Review Letters*, **6**, 47-48. https://doi.org/10.1103/physrevlett.6.47

[15] Gonzalez, W.D., Joselyn, J.A., Kamide, Y., Kroehl, H.W., Rostoker, G., Tsurutani, B.T., *et al.* (1994) What Is a Geomagnetic Storm? *Journal of Geophysical Research: Space Physics*, **99**, 5771-5792. https://doi.org/10.1029/93ja02867

[16] Von Humboldt, A. (1860) Cosmos: A Sketch of a Physical Description of the Universe. Volume 5, Harper.

[17] Burton, R.K., McPherron, R.L. and Russell, C.T. (1975) An Empirical Relationship between Interplanetary Conditions and *dst*. *Journal of Geophysical Research*, **80**, 4204-4214. https://doi.org/10.1029/ja080i031p04204

[18] Daglis, I.A., Thorne, R.M., Baumjohann, W. and Orsini, S. (1999) The Terrestrial Ring Current: Origin, Formation, and Decay. *Reviews of Geophysics*, **37**, 407-438. https://doi.org/10.1029/1999rg900009

[19] Rostoker, G. (1972) Geomagnetic Indices. *Reviews of Geophysics*, **10**, 935-950. https://doi.org/10.1029/rg010i004p00935

[20] Xue, D., Wu, L., Xu, T., Wu, C., Wang, Z. and He, Z. (2024) Space Weather Effects on Transportation Systems: A Review of Current Understanding and Future Outlook. *Space Weather*, **22**, e2024SW004055. https://doi.org/10.1029/2024sw004055

[21] Mansilla, G.A. and Zossi, M.M. (2013) Ionospheric Response to the 3 August 2010 Geomagnetic Storm at Mid and Mid-High Latitudes. *Advances in Space Research*, **51**, 50-60. https://doi.org/10.1016/j.asr.2012.09.001

[22] Liu, W., Xu, L., Xiong, C. and Xu, J. (2017) The Ionospheric Storms in the American Sector and Their Longitudinal Dependence at the Northern Middle Latitudes. *Advances in Space Research*, **59**, 603-613. https://doi.org/10.1016/j.asr.2016.10.032

[23] de Abreu, A.J., Correia, E., de Jesus, R., Venkatesh, K., Macho, E.P., Roberto, M., *et al.* (2023) Statistical Analysis on the Ionospheric Response over South American Mid- and Near High-Latitudes during 70 Intense Geomagnetic Storms Occurred in the Period of Two Decades. *Journal of Atmospheric and Solar-Terrestrial Physics*, **245**, Article ID: 106060. https://doi.org/10.1016/j.jastp.2023.106060

[24] Kamide, Y., Sun, W. and Akasofu, S. (1996) The Average Ionospheric Electrodynamics for the Different Substorm Phases. *Journal of Geophysical Research: Space Physics*, **101**, 99-109. https://doi.org/10.1029/95ja02990

[25] Amabayo, E.B., McKinnell, L. and Cilliers, P.J. (2012) Ionospheric Response over South Africa to the Geomagnetic Storm of 11-13 April 2001. *Journal of Atmospheric and Solar-Terrestrial Physics*, **84**, 62-74. https://doi.org/10.1016/j.jastp.2012.06.002

[26] Tsurutani, B.T. and Lakhina, G.S. (2014) An Extreme Coronal Mass Ejection and

Consequences for the Magnetosphere and Earth. *Geophysical Research Letters*, **41**, 287-292. https://doi.org/10.1002/2013gl058825

[27] Nayak, C., Tsai, L., Su, S., Galkin, I.A., Tan, A.T.K., Nofri, E., *et al.* (2016) Peculiar Features of the Low-latitude and Midlatitude Ionospheric Response to the St. Patrick's Day Geomagnetic Storm of 17 March 2015. *Journal of Geophysical Research*: *Space Physics*, **121**, 7941-7960. https://doi.org/10.1002/2016ja022489

[28] Hofmann-Wellenhof, B., Lichtenegger, H. and Collins, J. (2012) Global Positioning System: Theory and Practice. Springer Science & Business Media.

[29] Kintner, P.M., Ledvina, B.M. and de Paula, E.R. (2007) GPS and Ionospheric Scintillations. *Space Weather*, **5**, S09003. https://doi.org/10.1029/2006sw000260

[30] Astafyeva, E. (2019) Ionospheric Detection of Natural Hazards. *Reviews of Geophysics*, **57**, 1265-1288. https://doi.org/10.1029/2019rg000668

[31] Astafyeva, E., Zakharenkova, I. and Förster, M. (2015) Ionospheric Response to the 2015 St. Patrick's Day Storm: A Global Multi-Instrumental Overview. *Journal of Geophysical Research*: *Space Physics*, **120**, 9023-9037. https://doi.org/10.1002/2015ja021629

[32] Seaton, M.J. (1956) A Possible Explanation of the Drop in F-Region Critical Densities Accompanying Major Ionospheric Storms. *Journal of Atmospheric and Terrestrial Physics*, **8**, 122-124.

[33] Mendillo, M., Klobuchar, J.A. and Hajeb-Hosseinieh, H. (1974) Ionospheric Disturbances: Evidence for the Contraction of the Plasmasphere during Severe Geo-Magnetic Storms. *Planetary and Space Science*, **22**, 223-236. https://doi.org/10.1016/0021-9169(56)90102-7.

[34] Zhao, B., Wan, W., Tschu, K., Igarashi, K., Kikuchi, T., Nozaki, K., *et al.* (2008) Ionosphere Disturbances Observed Throughout Southeast Asia of the Superstorm of 20-22 November 2003. *Journal of Geophysical Research*: *Space Physics*, **113**, A00A04. https://doi.org/10.1029/2008ja013054

[35] Amaechi, P.O., Oyeyemi, E.O. and Akala, A.O. (2018) Geomagnetic Storm Effects on the Occurrences of Ionospheric Irregularities over the African Equatorial/Low-Latitude Region. *Advances in Space Research*, **61**, 2074-2090. https://doi.org/10.1016/j.asr.2018.01.035

[36] Kappenman, J.G. (1996) Geomagnetic Storms and Their Impact on Power Systems. *IEEE Power Engineering Review*, **16**, 5. https://doi.org/10.1109/mper.1996.491910

[37] Akala, A.O., Doherty, P.H., Carrano, C.S., Valladares, C.E. and Groves, K.M. (2012) Impacts of Ionospheric Scintillations on GPS Receivers Intended for Equatorial Aviation Applications. *Radio Science*, **47**, RS4007. https://doi.org/10.1029/2012rs004995

[38] Luo, X., Gu, S., Lou, Y., Xiong, C., Chen, B. and Jin, X. (2018) Assessing the Performance of GPS Precise Point Positioning under Different Geomagnetic Storm Conditions during Solar Cycle 24. *Sensors*, **18**, Article No. 1784. https://doi.org/10.3390/s18061784

[39] Bojilova, R. and Mukhtarov, P. (2023) Analysis of the Ionospheric Response to Sudden Stratospheric Warming and Geomagnetic Forcing over Europe during February and March 2023. *Universe*, **9**, Article No. 351. https://doi.org/10.3390/universe9080351

[40] Habarulema, J.B., McKinnell, L. and Opperman, B.D.L. (2010) TEC Measurements and Modelling over Southern Africa during Magnetic Storms; a Comparative Analysis. *Journal of Atmospheric and Solar-Terrestrial Physics*, **72**, 509-520. https://doi.org/10.1016/j.jastp.2010.01.012

[41] Tshisaphungo, M., Habarulema, J.B. and McKinnell, L.-A. (2018) Modeling Ionospheric foF2 Response during Geomagnetic Storms Using Neural Network and Linear Regression Techniques. *Advances in Space Research*, **61**, 2891-2903.

[42] Gulyaeva, T.L. and Bilitza, D. (2012) Towards ISO Standard Earth Ionosphere and Plasmasphere Model. In: Larsen, R.J., Ed., *New Developments in the Standard Model*, Nova Science Publishers, 1-39.

[43] Seemala, G.K. and Valladares, C.E. (2011) Statistics of Total Electron Content Depletions Observed over the South American Continent for the Year 2008. *Radio Science*, **46**, RS5019. https://doi.org/10.1029/2011rs004722

[44] Klobuchar, J. (1987) Ionospheric Time-Delay Algorithm for Single-Frequency GPS Users. *IEEE Transactions on Aerospace and Electronic Systems*, **23**, 325-331. https://doi.org/10.1109/taes.1987.310829

[45] Ma, G. and Maruyama, T. (2003) Derivation of TEC and Estimation of Instrumental Biases from GEONET in Japan. *Annales Geophysicae*, **21**, 2083-2093. https://doi.org/10.5194/angeo-21-2083-2003

[46] Habyarimana, V., Habarulema, J.B., Okoh, D., Dugassa, T. and Uwamahoro, J.C. (2023) Single Station Modelling of Ionospheric Irregularities Using Artificial Neural Networks. *Astrophysics and Space Science*, **368**, Article No. 105. https://doi.org/10.1007/s10509-023-04261-8

[47] Liu, L., Wan, W., Ning, B., Pirog, O.M. and Kurkin, V.I. (2006) Solar Activity Variations of the Ionospheric Peak Electron Density. *Journal of Geophysical Research*: *Space Physics*, **111**, A08304. https://doi.org/10.1029/2006ja011598

[48] Gonzalez, W.D., Tsurutani, B.T. and Clúa de Gonzalez, A.L. (1999) Interplanetary Origin of Geomagnetic Storms. *Space Science Reviews*, **88**, 529-562. https://doi.org/10.1023/a:1005160129098

[49] Ebihara, Y. and Ejiri, M. (2000) Simulation Study on Fundamental Properties of the Storm-Time Ring Current. *Journal of Geophysical Research*: *Space Physics*, **105**, 15843-15859. https://doi.org/10.1029/1999ja900493

[50] Tsurutani, B.T., Gonzalez, W.D., Gonzalez, A.L.C., Guarnieri, F.L., Gopalswamy, N., Grande, M., *et al.* (2006) Corotating Solar Wind Streams and Recurrent Geomagnetic Activity: A Review. *Journal of Geophysical Research*: *Space Physics*, **111**, A07S01. https://doi.org/10.1029/2005ja011273

[51] Zhang, J., Richardson, I.G., Webb, D.F., Gopalswamy, N., Huttunen, E., Kasper, J.C., *et al.* (2007) Solar and Interplanetary Sources of Major Geomagnetic Storms ($Dst \leq -100$ Nt) during 1996-2005. *Journal of Geophysical Research*: *Space Physics*, **112**, A10102. https://doi.org/10.1029/2007ja012321

[52] Habyarimana, V., Habarulema, J.B. and Dugassa, T. (2023) Analysis of Ionospheric Storm-Time Effects over the East African Sector during the 17 March 2013 and 2015 Geomagnetic Storms. *Earth, Planets and Space*, **75**, Article No. 58. https://doi.org/10.1186/s40623-023-01812-9

[53] Rishbeth, H. and Setty, C.S.G.K. (1961) The F-Layer at Sunrise. *Journal of Atmospheric and Terrestrial Physics*, **20**, 263-276. https://doi.org/10.1016/0021-9169(61)90205-7

[54] Picanço, G.A.S., Denardini, C.M., Nogueira, P.A.B., Barbosa-Neto, P.F., Resende, L.C.A., Chen, S.S., *et al.* (2021) Equatorial Ionospheric Response to Storm-Time Electric Fields during Two Intense Geomagnetic Storms over the Brazilian Region Using a Disturbance Ionosphere Index. *Journal of Atmospheric and Solar-Terrestrial Physics*, **223**, Article ID: 105734. https://doi.org/10.1016/j.jastp.2021.105734

[55] Willmott, C. and Matsuura, K. (2005) Advantages of the Mean Absolute Error (MAE) over the Root Mean Square Error (RMSE) in Assessing Average Model Performance. *Climate Research*, **30**, 79-82. https://doi.org/10.3354/cr030079

[56] Uwamahoro, J.C. and Habarulema, J.B. (2015) Modelling Total Electron Content during Geomagnetic Storm Conditions Using Empirical Orthogonal Functions and Neural Networks. *Journal of Geophysical Research*: *Space Physics*, **120**, 11,000-11,012. https://doi.org/10.1002/2015ja021961

[57] Borovsky, J.E. and Denton, M.H. (2006) Differences between CME-Driven Storms and CIR-Driven Storms. *Journal of Geophysical Research*: *Space Physics*, **111**, A07S08. https://doi.org/10.1029/2005ja011447

[58] Habarulema, J.B., Katamzi, Z.T. and Yizengaw, E. (2014) A Simultaneous Study of Ionospheric Parameters Derived from FORMOSAT-3/COSMIC, GRACE, and CHAMP Missions over Middle, Low, and Equatorial Latitudes: Comparison with Ionosonde Data. *Journal of Geophysical Research*: *Space Physics*, **119**, 7732-7744. https://doi.org/10.1002/2014ja020192